

Ref-DGS: Reflective Dual Gaussian Splatting

NINGJING FAN, Chongqing University, China

YIQUN WANG, Chongqing University, France

DONGMING YAN, Institute of Automation, Chinese Academy of Sciences, China

PETER WONKA, King Abdullah University of Science and Technology (KAUST), Saudi Arabia

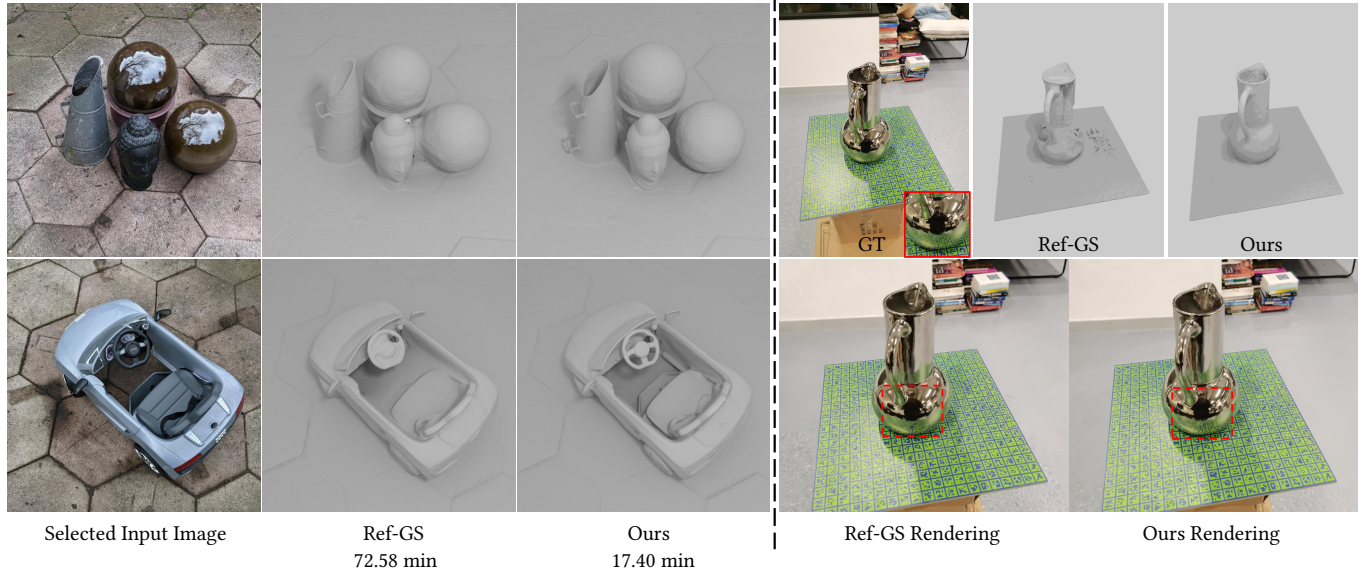


Fig. 1. **Left:** Surface reconstruction results on the RefReal dataset for two challenging scenes, gardenspheres (top) and toycar (bottom), both with strong near-field specular reflections. The bottom row reports the average training time. **Right:** Results on the GlossyReal dataset for the vase scene, showing surface reconstruction and rendering quality. Our method produces more accurate geometry and higher-quality reflections, as highlighted in the close-up regions.

Reflective appearance, especially strong and typically near-field specular reflections, poses a fundamental challenge for accurate surface reconstruction and novel view synthesis. Existing Gaussian splatting methods either fail to model near-field specular reflections or rely on explicit ray tracing at substantial computational cost. We present **Ref-DGS**, a reflective dual Gaussian splatting framework that addresses this trade-off by decoupling surface reconstruction from specular reflection within an efficient rasterization-based pipeline. Ref-DGS introduces a dual Gaussian scene representation consisting of geometry Gaussians and complementary local reflection Gaussians that capture near-field specular interactions without explicit ray tracing, along with a global environment reflection field for modeling far-field specular reflections. To predict specular radiance, we further propose a lightweight, physically-aware adaptive mixing shader that fuses global and local reflection features. Experiments demonstrate that Ref-DGS achieves state-of-the-art performance on reflective scenes while training substantially faster than ray-based Gaussian methods.

CCS Concepts: • **Computing methodologies** → **Computer vision**; **Artificial intelligence**; **Computer graphics**.

Additional Key Words and Phrases: Gaussian Splatting, Reflective Appearance, Surface Reconstruction, Novel View Synthesis

Authors' Contact Information: Ningjing Fan, Chongqing University, China; Yiqun Wang, Chongqing University, France; Dongming Yan, Institute of Automation, Chinese Academy of Sciences, China; Peter Wonka, King Abdullah University of Science and Technology (KAUST), Saudi Arabia.

1 Introduction

Scenes with reflective materials pose significant challenges for surface reconstruction and novel view synthesis, as view-dependent specular and indirect effects violate the multi-view appearance consistency assumptions commonly used for geometry recovery and rendering. While recent neural rendering methods achieve impressive results for predominantly diffuse scenes, faithfully handling specular reflections and view-dependent effects under complex lighting remains difficult, especially when high visual quality and practical training efficiency are both required. NeRF-based approaches address view-dependent appearance through volumetric radiance fields and physically inspired shading [Mildenhall et al. 2020], but their reliance on dense ray sampling and volumetric integration leads to high computational cost and limited scalability. In contrast, 3D Gaussian Splatting (3DGS) has emerged as an efficient alternative, enabling fast novel view synthesis via differentiable rasterization [Kerbl et al. 2023]. However, extending Gaussian-based representations to jointly support accurate surface reconstruction and faithful modeling of reflective effects within an efficient rasterization-based framework remains an open problem.

At the core of this difficulty lies a mismatch between the physical nature of specular reflection and the representations used in existing Gaussian-based methods. A large body of work [Chen et al. 2024; Guédon et al. 2025; Huang et al. 2024a; Yu et al. 2024b] focuses on

improving surface reconstruction quality, achieving accurate and stable geometry but without explicitly modeling specular reflection. In reflective scenes, view-dependent specular effects are therefore absorbed into the geometry during optimization, leading to surface shrinkage, local dents, and the loss of high-frequency details. Other approaches introduce explicit specular modeling within a Gaussian splatting framework [Jiang et al. 2024; Yang et al. 2024; Ye et al. 2024; Zhang et al. 2025a], typically by querying environment illumination or using single-bounce reflection models. While effective for far-field reflections, these models fail to capture near-field specular reflections, such as self-reflections and geometry-induced inter-reflections, which are often prominent on glossy surfaces. More recent methods [Gao et al. 2024; Xie et al. 2025; Yao et al. 2025; Zhang et al. 2025c; Zhu et al. 2025] address this limitation by incorporating ray tracing to model near-field inter-reflections. Although physically accurate, this strategy incurs substantial computational overhead and significantly slows training, eroding the efficiency advantages that make Gaussian splatting attractive. Fundamentally, these limitations stem from attempting to encode both view-invariant geometry and complex view-dependent specular reflection within a single representation, forcing incompatible phenomena to be explained by the same parameters.

In this paper, we present **Ref-DGS**, a reflective dual Gaussian splatting framework that addresses two fundamental limitations of existing Gaussian-based rendering methods. First, we show that reflective appearance should not be treated as a geometric property: forcing view-dependent specular effects into surface-aligned Gaussians leads to unstable geometry and degraded surface reconstruction. Second, we demonstrate that explicitly separating specular reflection from geometry does not require costly ray tracing to model near-field inter-reflections within objects, which significantly undermines the efficiency advantages of Gaussian splatting. To resolve these issues, Ref-DGS introduces a dual Gaussian scene representation that assigns geometry and near-field specular reflections to two complementary sets of Gaussians, enabling reflective appearance modeling within an efficient rasterization-based pipeline. Far-field global reflections are handled via environment-based illumination, while near-field local reflections are captured using rasterization-friendly local reflection features and integrated through a lightweight, physically-aware adaptive mixing shader. This design preserves the efficiency and stability of Gaussian splatting while enabling faithful reflective appearance modeling, achieving state-of-the-art performance in both surface reconstruction and novel view synthesis, with substantially faster training than ray-based Gaussian methods.

In summary, our contributions are:

- A reflective dual Gaussian splatting framework that introduces a *dual Gaussian scene representation* to explicitly disentangle near-field specular reflections from surface geometry, assigning local reflective interactions to a dedicated set of local reflection Gaussians and enabling efficient reflective appearance modeling without explicit ray tracing.
- A *global-local reflection representation* that models specular appearance using two complementary components: global

reflection features capturing far-field environment illumination, and local reflection features extracted from the local reflection Gaussians to represent near-field inter-reflections.

- A lightweight *physically-aware adaptive mixing shader* that fuses global and local reflection features conditioned on material roughness and geometric angular factors, enabling fast convergence and state-of-the-art performance in both surface reconstruction and novel view synthesis.

2 Related Work

We review prior work on novel view synthesis and surface reconstruction, with a focus on neural and Gaussian-based scene representations and their treatment of reflective appearance.

2.1 Novel View Synthesis

Novel view synthesis aims to render photorealistic images from unseen viewpoints. NeRF-based approaches [Barron et al. 2021, 2022; Mildenhall et al. 2020] achieve high-quality view synthesis but incur high training and rendering costs due to volumetric ray marching. To improve efficiency, factorized or explicit scene representations have been proposed, including Plenoxels [Fridovich-Keil et al. 2022], TensoRF [Chen et al. 2022], and Instant-NGP [Müller et al. 2022].

3D Gaussian Splatting (3DGS) [Kerbl et al. 2023] further improves efficiency by representing scenes with explicit Gaussian primitives and enabling fast rasterization-based rendering. Building upon this framework, subsequent works extend Gaussian splatting to better handle reflective appearance and complex illumination in novel view synthesis, by incorporating view-dependent components, near-field illumination modeling, deferred shading, or explicit reflective transport [Gao et al. 2024; Jiang et al. 2024; Liang et al. 2024; Xie et al. 2025; Yang et al. 2024; Yao et al. 2025; Ye et al. 2024; Zhang et al. 2025c,a]. These approaches improve visual fidelity under challenging lighting conditions, at the cost of increased computational complexity. In addition, many surface reconstruction works reviewed in the following subsection also support reflective novel view synthesis.

2.2 Surface Reconstruction

Volumetric surface reconstruction with neural fields. Surface reconstruction is a core problem in neural rendering. NeRF-based methods and implicit signed distance field (SDF) formulations represent scenes as continuous volumetric fields and have been widely adopted for accurate geometry reconstruction [Mildenhall et al. 2020; Wang et al. 2021]. Several extensions incorporate reflective appearance and view-dependent effects through physically inspired shading or radiance decomposition [Fan et al. 2025; Ge et al. 2023; Li et al. 2024; Liang et al. 2023; Liu et al. 2023; Verbin et al. 2022; Wang et al. 2024]. Despite their high reconstruction quality, these methods rely on dense ray sampling and volumetric integration, resulting in high computational cost and limited scalability.

Gaussian-based surface reconstruction in predominantly diffuse scenes. Gaussian-based representations provide an efficient alternative to volumetric formulations for surface reconstruction. SuGaR [Guédon and Lepetit 2024], PGSR [Chen et al. 2024], and GOF [Yu et al. 2024b] improve geometric fidelity within the Gaussian framework through enhanced depth estimation and geometric regularization.

Other approaches, such as NeuSG [Chen et al. 2023], GSDF [Yu et al. 2024a], and 3DGS [Lyu et al. 2024], integrate Gaussian representations with signed distance fields to enable explicit surface reconstruction. In parallel, surface-aware Gaussian formulations progressively enhance geometric expressiveness, where 2D Gaussian Splatting (2DGS) [Huang et al. 2024a] introduces local surface parameterization, and Quadratic Gaussian Splatting (QGS) [Zhang et al. 2025b] further extends this formulation with deformable quadric primitives and geometry-aware density modeling to better capture complex surface curvature. In a different direction, MLo [Guédon et al. 2025] jointly optimizes Gaussians and an explicitly extracted mesh by enforcing bidirectional consistency between the two representations, enabling synchronized geometry refinement without introducing an additional SDF representation.

Gaussian-based surface reconstruction in reflective scenes. Surface reconstruction becomes more challenging in the presence of reflective appearance, as view-dependent specular and indirect effects violate appearance consistency assumptions commonly used for geometry recovery. To address this, several works extend Gaussian splatting to better account for reflective effects during reconstruction and rendering. GaussianShader [Jiang et al. 2024] and SpecGaussian [Yang et al. 2024] introduce explicit specular components within the Gaussian framework, primarily targeting far-field or direct reflections. Deferred rendering formulations further decouple geometry and shading to improve reconstruction robustness under complex illumination, as explored in 3DGS-DR [Ye et al. 2024] and Ref-GS [Zhang et al. 2025a]. To capture near-field inter-reflections, GS-IR [Liang et al. 2024] represents reflective transport using spherical harmonic features, while Ref-Gaussian [Yao et al. 2025], EnvGS [Xie et al. 2025], and MaterialRefGS [Zhang et al. 2025c] incorporate explicit ray tracing to model near-field reflective interactions, at the cost of increased computational overhead. GS-ROR² further addresses surface reconstruction in reflective scenes by bidirectionally coupling 3D Gaussian splatting with signed distance fields, leveraging mutual depth and normal supervision to jointly enable efficient relighting and high-quality geometry reconstruction. Overall, these approaches explore different trade-offs between geometric fidelity, reflective expressiveness, and computational efficiency.

3 Method

This section presents the proposed reflective dual Gaussian splatting framework. We first review 2D Gaussian splatting as the foundation of our approach (Sec. 3.1). We then describe the dual Gaussian splatting framework, including the dual Gaussian scene representation (Sec. 3.2.1), the construction of global and local specular features (Sec. 3.2.2), and a physically-aware specular adaptive mixing shader (Sec. 3.2.3).

3.1 Gaussian Splatting

Our method builds upon 2D Gaussian Splatting (2DGS) [Huang et al. 2024b], which represents a scene as a collection of planar Gaussian surface primitives and renders them using a fast, fully differentiable splatting rasterizer. Compared to vanilla 3DGS [Kerbl et al. 2023], 2DGS constrains each primitive to a local tangent disk, yielding a surface-aligned representation that is better suited for

thin structures and for producing reliable geometric information such as depth and surface normals.

Each surface primitive is parameterized by a 3D center $\mathbf{p}_k \in \mathbb{R}^3$, an opacity $\alpha_k \in (0, 1)$, and a local planar Gaussian defined by a rotation matrix $\mathbf{R}_k = [\mathbf{t}_{u,k}, \mathbf{t}_{v,k}, \mathbf{t}_{w,k}]$, where $\mathbf{t}_{u,k}$ and $\mathbf{t}_{v,k}$ are orthogonal tangential directions and $\mathbf{t}_{w,k} = \mathbf{t}_{u,k} \times \mathbf{t}_{v,k}$, and a diagonal scaling matrix $\mathbf{S}_k = \text{diag}(s_{u,k}, s_{v,k}, 0)$. A point on the local tangent disk is expressed in local coordinates as

$$\mathbf{P}_k(u, v) = \mathbf{p}_k + s_{u,k} \mathbf{t}_{u,k} u + s_{v,k} \mathbf{t}_{v,k} v, \quad (1)$$

where (u, v) denote normalized local coordinates on the disk. The corresponding Gaussian weight is defined as a unit-variance isotropic Gaussian in the local parameter space,

$$\mathcal{G}(u, v) = \exp\left(-\frac{u^2 + v^2}{2}\right). \quad (2)$$

Following the standard splatting formulation [Huang et al. 2024b; Kerbl et al. 2023], each planar Gaussian projects to an anisotropic ellipse in screen space through perspective projection and local linearization. The ellipse is evaluated within a conservative bounding box and organized into screen-space tiles for efficient rasterization. Primitives are depth-sorted by their centers and composited in a front-to-back order using alpha compositing:

$$\mathbf{c}(\mathbf{q}) = \sum_{k=1}^K c_k \alpha_k \hat{\mathcal{G}}_k(\mathbf{q}) \prod_{j=1}^{k-1} (1 - \alpha_j \hat{\mathcal{G}}_j(\mathbf{q})), \quad (3)$$

where $\hat{\mathcal{G}}_k(\mathbf{q})$ denotes the projected 2D Gaussian kernel evaluated at pixel \mathbf{q} , and c_k represents a per-primitive attribute such as color or a learnable feature. Rendering terminates early once the accumulated opacity saturates, and the entire process is fully differentiable with respect to both geometric parameters and per-primitive attributes.

3.2 Dual Gaussian Splatting

We propose a dual Gaussian splatting framework that combines far-field environment reflections obtained by querying a learnable spherical feature map using the spherical mipmap (Sph-Mip) encoding with near-field specular effects captured by an auxiliary set of Gaussian particles. The global and local specular features are subsequently fused by a physically-aware shader to predict specular radiance. An overview of our framework is shown in Fig. 2.

3.2.1 Dual Gaussian Scene Representation. Building on the 2D Gaussian splatting (Sec. 3.1), we introduce a dual Gaussian scene representation that decomposes the scene into two complementary sets of Gaussians with distinct roles: the geometry Gaussians \mathcal{G}_{geo} and the local reflection Gaussians $\mathcal{G}_{\text{local}}$.

Geometry Gaussians \mathcal{G}_{geo} . The geometry Gaussians are designed to capture view-independent scene structure and to provide stable geometric information for rendering and surface reconstruction. Each primitive in \mathcal{G}_{geo} follows the 2DGS formulation and is augmented with material-related attributes, including diffuse color and surface roughness, which are treated as view-invariant properties tied to the underlying geometry. When splatted, \mathcal{G}_{geo} produces screen-space attribute maps such as diffuse color $\mathbf{C}_{\text{diff}}(\mathbf{p})$ and roughness $\rho(\mathbf{p})$, together with geometric information including depth and

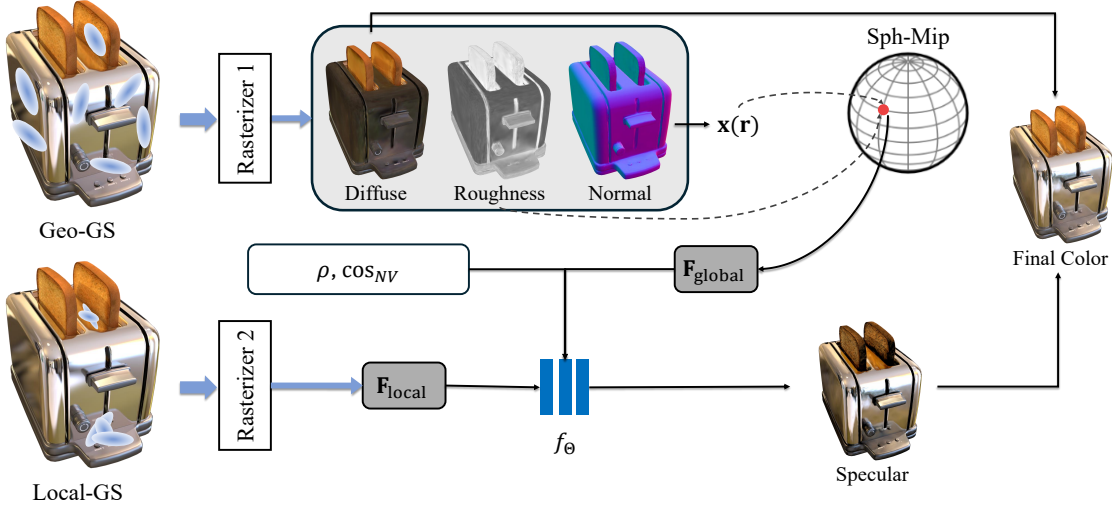


Fig. 2. An overview of our Ref-DGS framework.

surface normals. These maps are used as inputs to the subsequent shading stages and reflection modeling.

Local reflection Gaussians $\mathcal{G}_{\text{local}}$. The local reflection Gaussians are introduced to model local, view-dependent specular reflection effects arising from nearby geometry. Each primitive in $\mathcal{G}_{\text{local}}$ stores a learnable local reflection feature $f \in \mathbb{R}^d$. Splatting $\mathcal{G}_{\text{local}}$ produces the corresponding screen-space feature map $F_{\text{local}}(\mathbf{p})$. Intuitively, F_{local} provides a compact implicit representation of self-reflections and inter-reflections, enabling efficient modeling of near-field specular reflections within a rasterization-based and fully differentiable framework. It is important that these Gaussians do not influence and thereby distort the surface reconstruction, which is handled solely by the geometry Gaussians.

3.2.2 Global-Local Specular Features. For each pixel \mathbf{p} , we construct specular features by combining (i) far-field global reflection features obtained by querying a learnable spherical feature map using the spherical mipmap (Sph-Mip) encoding, and (ii) near-field local reflection features rendered from the local reflection Gaussians $\mathcal{G}_{\text{local}}$.

Far-field global specular reflection via Sph-Mip. Following Ref-GS [Zhang et al. 2025a], we represent far-field specular reflections using a learnable spherical feature map \mathbf{M} . Far-field global reflection features are obtained by applying the Sph-Mip encoding, which queries \mathbf{M} conditioned on the reflection direction and surface roughness. For each pixel, we compute the specular reflection direction \mathbf{r} from the estimated surface normal and view direction, convert it to spherical coordinates $\mathbf{x}(\mathbf{r}) \in [0, 1]^2$, and select a roughness-dependent mipmap level:

$$F_{\text{global}}(\mathbf{p}) = \text{Sph-Mip}(\mathbf{x}(\mathbf{r}), \ell(\rho(\mathbf{p})), \mathbf{M}), \quad (4)$$

where $F_{\text{global}}(\mathbf{p}) \in \mathbb{R}^d$, and $\ell(\cdot)$ maps surface roughness to a continuous mipmap level to approximate prefiltered far-field specular reflections from the environment.

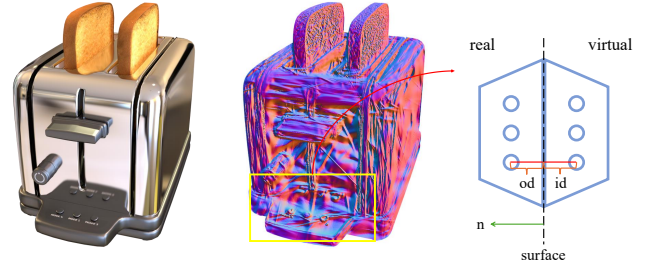


Fig. 3. **Left:** Input image. **Middle:** Normal map of the local reflection Gaussians $\mathcal{G}_{\text{local}}$. **Right:** Illustration of specular reflection, where the surface normal \mathbf{n} is perpendicular to the surface, and the image distance (id) equals the object distance (od).

Near-field local specular reflection from $\mathcal{G}_{\text{local}}$. We render the local reflection Gaussians $\mathcal{G}_{\text{local}}$ to obtain per-pixel local specular features

$$F_{\text{local}}(\mathbf{p}) \in \mathbb{R}^d, \quad (5)$$

which captures near-field specular reflection effects that are difficult to represent using a global environment model alone.

The global and local specular features are subsequently fused by the specular shader described in Sec. 3.2.3.

Discussion. We justify the necessity of the proposed local reflection Gaussians by analyzing the physical properties of specular reflections. Attempting to encode local specular features directly into the geometry Gaussians \mathcal{G}_{geo} is problematic due to the depth discrepancy between the physical surface and the mirror-induced virtual image on a glossy surface. As illustrated in Fig. 3 (right), according to the law of specular reflection for a planar mirror, the image distance (id) equals the object distance (od), implying that the virtual image lies "behind" the reflective surface. This effect is visualized in Fig. 3, where the normal map of the local reflection Gaussians $\mathcal{G}_{\text{local}}$ exhibits a concave structure extending inward from the physical surface, explicitly modeling the virtual reflection geometry. Without such decoupling, the geometry representation

	ball	car	coffee	helmet	teapot	toaster	mean	time↓
Ref-NeRF	1.55	14.93	12.24	29.48	9.23	42.87	18.38	–
ENVIDR	0.74	7.10	9.23	1.66	2.47	6.45	4.61	–
UniSDF	0.45	6.88	8.00	1.72	2.80	6.45	8.71	–
PGSR	66.93	4.62	2.91	6.01	1.01	15.31	16.13	27.5m
MiLo	61.30	4.47	2.36	4.87	0.62	16.49	15.02	18.9m
GaussianShader	7.03	14.05	14.93	9.33	7.17	13.08	10.93	1.10h
3DGS-DR	0.85	2.32	2.21	1.67	0.53	6.99	2.43	26.5m
Ref-Gaussian	0.71	1.91	2.34	1.85	0.48	5.70	2.17	35.9m
Ref-GS	1.05	2.02	3.61	1.99	0.69	3.92	2.21	23.5m
GS-ROR ²	0.47	2.06	5.47	1.82	0.52	5.52	2.64	1.34h
MaterialRefGS	0.63	1.86	1.79	1.46	0.44	7.02	2.20	2.42h
Ours	0.61	1.72	1.86	1.35	0.58	2.43	1.43	12.6m

Table 1. Quantitative surface reconstruction comparison on the ShinySynthetic dataset (normal MAE and training time). Best results are highlighted in red and second-best in yellow.

would be forced to collapse inward to match the virtual depth in order to reproduce specular appearance, leading to degraded surface reconstruction. By separating local reflection from geometry, our approach preserves surface correctness while enabling high-fidelity specular rendering. Moreover, by avoiding explicit ray tracing, our approach maintains fast training speed and enables robust novel view synthesis, since mirror-induced virtual images are explicitly modeled as local Gaussians located behind the physical surface and shift naturally across the image as the camera viewpoint changes.

3.2.3 Physically-Aware Specular Adaptive Mixing Shader. We predict specular radiance using a neural shader that combines two key ingredients: an adaptive mixing mechanism that balances global and local specular features, and physically-aware conditioning that enforces view-dependent reflectance behavior.

Adaptive mixing of global and local features. We provide the shader with two complementary specular features that characterize specular reflection at different spatial scales. The global specular features $\mathbf{F}_{\text{global}}(\mathbf{p})$ capture far-field environment reflections, while the local specular features $\mathbf{F}_{\text{local}}(\mathbf{p})$ account for near-field effects such as self-reflections and geometry-induced inter-reflections. Since their relative importance varies spatially and across viewpoints (e.g., open regions are dominated by environmental reflections, whereas concavities and self-occluding areas rely more on local reflections), the shader learns a view- and material-dependent mixing strategy evaluated per pixel. This adaptive mixing is learned implicitly through the joint utilization of $\mathbf{F}_{\text{global}}(\mathbf{p})$ and $\mathbf{F}_{\text{local}}(\mathbf{p})$ in the final specular prediction.

Physically-aware conditioning. We take physically motivated geometric and material terms as explicit conditioning inputs, as they capture the key factors governing view-dependent reflection. Specifically, we use the surface roughness $\rho(\mathbf{p})$ and the cosine between the surface normal \mathbf{n} and the view direction \mathbf{v} ,

$$\cos_{NV} = \max(\mathbf{n} \cdot \mathbf{v}, 0), \quad (6)$$

which are concatenated with the specular features to guide the shading process.

Specular shading. The final specular radiance is predicted by a single MLP that takes as input the global and local specular features together with the physically-aware conditioning terms:

$$\mathbf{C}_{\text{spec}}(\mathbf{p}) = f_{\Theta}(\mathbf{F}_{\text{global}}(\mathbf{p}), \mathbf{F}_{\text{local}}(\mathbf{p}), \rho(\mathbf{p}), \cos_{NV}). \quad (7)$$

	angel	bell	cat	horse	luyu	potion	tbell	teapot	mean
CD↓									
PGSR	0.77	3.08	3.39	0.90	1.16	3.99	4.59	4.57	2.81
MiLo	0.77	16.52	2.84	1.02	44.64	3.39	5.08	4.40	9.83
GaussianShader	0.85	1.10	2.56	0.73	1.07	4.74	5.74	3.40	2.53
Ref-Gaussian	0.45	0.70	1.68	0.64	0.88	0.81	0.59	1.01	0.95
Ref-GS	0.41	0.74	1.73	0.47	0.89	1.05	0.52	0.88	0.84
GS-ROR ²	0.52	0.32	1.66	0.46	0.92	0.86	0.58	0.66	0.75
MaterialRefGS	0.53	0.70	1.97	0.47	0.96	0.62	0.55	1.02	0.85
Ours	0.38	0.65	0.93	0.42	0.64	0.66	0.52	0.79	0.62
MAE↓									
PGSR	4.90	6.39	8.43	5.97	5.91	11.12	12.62	6.28	7.70
MiLo	4.61	11.52	5.55	6.52	5.97	10.45	13.16	7.09	8.11
GaussianShader	2.90	1.60	4.33	3.27	4.56	9.52	5.60	3.01	4.35
3DGS-DR	4.46	4.53	4.64	6.59	5.65	4.44	5.39	3.38	4.89
Ref-Gaussian	1.79	1.16	3.15	4.03	3.15	3.04	2.02	1.20	2.44
Ref-GS	1.99	0.92	2.93	3.18	2.82	3.64	1.87	1.18	2.32
GS-ROR ²	2.09	0.86	3.37	2.85	3.15	4.04	2.64	1.04	2.51
MaterialRefGS	1.81	0.86	2.42	3.16	3.07	2.68	1.77	1.18	2.12
Ours	2.05	0.71	1.37	3.44	2.30	2.48	1.84	0.86	1.88

Table 2. Quantitative surface reconstruction comparison on the GlossySynthetic dataset (CD $\times 10^2$ and normal MAE). Best results are highlighted in red and second-best in yellow.

Given calibrated multi-view images $\{\mathbf{I}_o\}$ and known camera parameters, the pipeline renders a diffuse (base) component from the geometry Gaussians \mathcal{G}_{geo} and a specular component predicted by the shader. The final linear color at pixel \mathbf{p} is given by

$$\mathbf{C}(\mathbf{p}) = \mathbf{C}_{\text{diff}}(\mathbf{p}) + \mathbf{C}_{\text{spec}}(\mathbf{p}). \quad (8)$$

For visualization, the linear RGB output is converted to sRGB by clamping to $[0, 1]$ followed by the standard transfer function:

$$\mathbf{C}_{\text{rgb}}(\mathbf{p}) = \text{sRGB}(\text{clamp}(\mathbf{C}(\mathbf{p}), 0, 1)), \quad (9)$$

where $\text{sRGB}(\cdot)$ denotes the canonical linear-to-sRGB conversion.

4 Experiments

4.1 Implementation Details

We jointly optimize the two sets of Gaussian primitives with associated features, following the same optimization and densification strategy as 2D Gaussian splatting (2DGS) [Huang et al. 2024b]. The Sph-Mip encoding uses a base level \mathbf{M} with resolution $H_{\mathbf{M}} = 512$, $W_{\mathbf{M}} = 1024$, and feature dimension $C = 4$, with $N = 9$ mipmap levels. The local reflection Gaussians $\mathcal{G}_{\text{local}}$ are associated with a local reflection feature $\mathbf{f} \in \mathbb{R}^4$. The physically-aware specular adaptive mixing shader is implemented as a lightweight MLP f_{Θ} with 3 hidden layers of width 64. All experiments are conducted on a single NVIDIA RTX 4090 GPU with 24 GB of memory.

4.2 Datasets, Baselines and Metrics

Datasets. We evaluate our method on two synthetic and two real-world datasets featuring glossy materials and complex specular transport. For synthetic experiments, we use ShinySynthetic [Verbin et al. 2022] and GlossySynthetic [Liu et al. 2023], which feature pronounced view-dependent reflections, high-frequency highlights, and strong near-field interactions, including self-reflections and inter-reflections. We additionally report results on the RefReal [Verbin et al. 2022] and GlossyReal [Liu et al. 2023] datasets to assess performance on real captures of reflective objects and scenes. For the RefReal dataset, we utilize 1/4 resolution for the gardenspheres

Datasets	ShinySynthetic			GlossySynthetic			Ref-Real		
	PSNR↑	SSIM↑	LPIPS↓	PSNR↑	SSIM↑	LPIPS↓	PSNR↑	SSIM↑	LPIPS↓
Ref-NeRF	33.32	0.956	0.110	25.65	0.905	0.112	23.62	0.646	0.239
ENVIDR	32.88	0.969	0.072	29.06	0.947	0.060	23.80	0.606	0.332
PGSR	26.82	0.921	0.119	25.59	0.913	0.091	24.43	0.696	0.220
MILo	27.28	0.921	0.124	25.69	0.914	0.096	23.87	0.643	0.291
GaussianShader	30.42	0.951	0.082	27.11	0.922	0.082	23.46	0.647	0.257
3DGS-DR	33.94	0.971	0.059	29.36	0.951	0.055	23.80	0.659	0.236
EnvGS	33.26	0.968	0.063	28.17	0.938	0.067	24.55	0.671	0.243
Ref-Gaussian	34.92	0.973	0.056	29.61	0.954	0.054	23.95	0.661	0.280
Ref-GS	34.80	0.973	0.056	30.37	0.960	0.048	23.93	0.655	0.267
GS-ROR ²	32.16	0.963	0.069	28.96	0.952	0.056	-	-	-
MaterialRefGS	34.16	0.972	0.058	30.74	0.961	0.047	-	-	-
Ours	35.21	0.975	0.053	30.63	0.958	0.052	24.89	0.697	0.224

Table 3. Quantitative NVS comparison. Best results are highlighted in red and second-best in yellow.

and toy car scenes, and 1/8 resolution for the sedan scene. For the GlossyReal dataset, all experiments are conducted at 1/4 resolution. Overall, these benchmarks present specular effects that are difficult to account for with a purely far-field environment model, making them well-suited for evaluating our global-local specular model.

Baselines. We compare our method against state-of-the-art baselines from both neural volume rendering and 3D Gaussian splatting (3DGS). For neural volume rendering, we include Ref-NeRF [Verbin et al. 2022], ENVIDR [Liang et al. 2023], and UniSDF [Wang et al. 2024]. For 3DGS-based methods, we evaluate PGSR [Chen et al. 2024], MILo [Guédon et al. 2025], GaussianShader [Jiang et al. 2024], 3DGS-DR [Ye et al. 2024], EnvGS [Xie et al. 2025], Ref-Gaussian [Yao et al. 2025], Ref-GS [Zhang et al. 2025a], GS-ROR² [Zhu et al. 2025], and MaterialRefGS [Zhang et al. 2025c]. MaterialRefGS [Zhang et al. 2025c] is included as a baseline, reproducing results strictly from the publicly available code at the time of submission.

Metrics. We assess geometric accuracy using the mean angular error (MAE) of surface normals and the chamfer distance (CD) between reconstructed and reference surfaces, and evaluate novel view synthesis quality using PSNR, SSIM, and LPIPS.

For geometry evaluation, we report only normal MAE on ShinySynthetic [Verbin et al. 2022] and both CD and normal MAE on GlossySynthetic [Liu et al. 2023]. As discussed in Ref-NeuS [Ge et al. 2023], the ground-truth meshes of ShinySynthetic contain two surface layers, while only the outer layer is visible in the input images, making completeness-based metrics such as CD unreliable due to dominant errors from invisible inner surfaces. For GlossySynthetic, since ground-truth surface normals are not provided, normal MAE is computed using normals derived from the ground-truth depth. Since the official implementation of GS-ROR² [Zhu et al. 2025] does not include geometry evaluation code, we apply a unified evaluation pipeline across all methods. Normal MAE and CD are computed following our procedure; for TSDF-based mesh extraction, we use a voxel size of 0.002 when computing CD.

4.3 Comparisons

Surface Reconstruction. We evaluate surface reconstruction quality on all datasets. Table 1 reports the normal MAE and training time on the ShinySynthetic [Verbin et al. 2022] dataset. Our method achieves the lowest reconstruction error while also exhibiting the fastest training time. Table 2 presents the CD and normal MAE on

the GlossySynthetic [Liu et al. 2023] dataset, where our method also outperforms competing approaches. Fig. 6 shows qualitative surface reconstruction results on both ShinySynthetic [Verbin et al. 2022] and GlossySynthetic [Liu et al. 2023] datasets. Our method reconstructs sharp and well-defined boundaries on thin structures, such as the edges of the spoon, and avoids the common failure of merging the coffee cup with its base caused by occlusions and cast shadows. In the toaster scene, which contains large front-facing surfaces dominated by near-field inter-reflections, our method produces smooth and coherent geometry without the surface indentations observed in competing methods. Similarly, in the cat scene, our approach prevents incorrect depth and normal estimation induced by inter-object light transport, successfully separating the object from the base while faithfully reconstructing fine structures such as the cat’s thin whiskers. Fig. 1 and Fig. 7 present qualitative surface reconstruction results on the RefReal [Verbin et al. 2022] and GlossyReal [Liu et al. 2023] datasets, respectively. In these real-world scenes with complex illumination and strong specular effects, our method reconstructs clean and consistent surfaces, preserving fine geometric details while avoiding spurious artifacts and surface distortions observed in competing methods.

A key challenge in the GlossyReal scenes, particularly the vase scene, is large specular reflections of nearby moving objects (e.g., the camera operator) observed on object surfaces. As these reflections vary across viewpoints, the effective far-field illumination changes dynamically with view. Existing methods often misinterpret such view-dependent specular reflections as geometric cues, leading to spurious surface deformations, such as indentations aligned with reflected silhouettes, even though the underlying illumination originates from the far field. In contrast, our method remains robust under these conditions and reconstructs reliable surfaces. This robustness can be attributed to our local reflection Gaussians $\mathcal{G}_{\text{local}}$ and their associated local specular features, which, beyond modeling near-field reflections, also adapt to complex, view-dependent variations in the environment illumination, preventing such effects from being incorrectly absorbed into the geometry.

Novel View Synthesis. We evaluate novel view synthesis performance on all datasets. Quantitative results are reported in Tab. 3, where our method consistently outperforms competing approaches. Fig. 8 shows qualitative results. In scenes containing strong near-field reflections, competing methods fail to reproduce view-consistent appearance, leading to blurred or distorted regions, while our method preserves coherent appearance under novel viewpoints. We do not report novel view synthesis results of GS-ROR² [Zhu et al. 2025] and MaterialRefGS [Zhang et al. 2025c] on the RefReal [Verbin et al. 2022] dataset, as GS-ROR² does not provide runnable code for this dataset, and the released implementation of MaterialRefGS is incomplete at the time of submission.

4.4 Ablation Studies

We conduct ablation studies on the ShinySynthetic [Verbin et al. 2022] and GlossySynthetic [Liu et al. 2023] datasets to validate the effectiveness of individual components. Quantitative ablation results are reported in Tab. 4. Qualitative results for surface reconstruction and novel view synthesis are shown in Fig. 9 and Fig. 10, respectively.

	PSNR↑	SSIM↑	LPIPS↓	MAE↓	CD↓	MAE↓
w/o F_{local} w/o G_{local}	34.36	0.971	0.057	1.53	0.82	1.99
w/o G_{local}	34.70	0.973	0.057	1.46	0.73	1.93
w/o Adap Mix	34.98	0.974	0.054	1.46	0.64	1.92
w/o Phy-Aware	35.02	0.975	0.053	1.45	0.62	1.90
Full model	35.21	0.975	0.053	1.43	0.62	1.88

Table 4. Ablation study on the ShinySynthetic (PSNR, SSIM, LPIPS, and normal MAE) and GlossySynthetic ($\text{CD} \times 10^2$ and normal MAE) datasets.

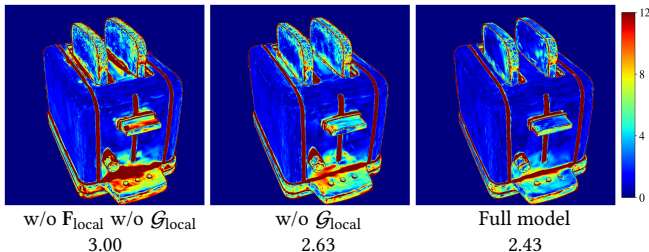


Fig. 4. Ablation on surface normal estimation. Angular error maps (red: high, blue: low) show that the full model significantly reduces geometric artifacts compared to ablated variants. Chamfer distances (CD) are reported at the bottom.

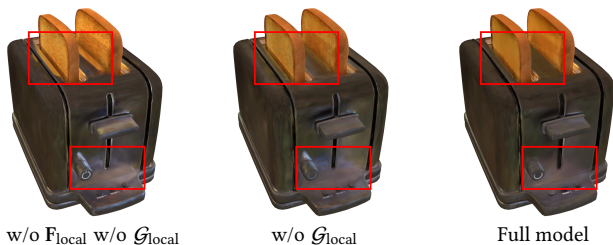


Fig. 5. Ablation study on the diffuse leakage issue, visualizing the predicted diffuse color.

Local Features. We ablate the local specular features by removing $F_{\text{local}}(\mathbf{p})$ and modeling specular appearance using only the global specular features $F_{\text{global}}(\mathbf{p})$. Accordingly, the local reflection Gaussians G_{local} are removed in this setting. This ablation evaluates the contribution of explicit near-field local reflection beyond far-field global reflection. As shown in Tab. 4, Fig. 4, Fig. 5, Fig. 9, and Fig. 10, when comparing w/o F_{local} w/o G_{local} and w/o G_{local} , removing the local specular features causes near-field specular reflections to be absorbed into the diffuse component, resulting in degraded geometry reconstruction and less accurate modeling of near-field specular effects.

Dual Gaussians. We ablate the dual Gaussian decomposition by removing the local reflection Gaussians G_{local} and instead deriving the local specular features $F_{\text{local}}(\mathbf{p})$ directly from the geometry Gaussians G_{geo} . This setting uses a single set of Gaussians to represent both geometry and near-field reflections, without the explicit decoupling between geometry and local reflections. As shown in Tab. 4, Fig. 9, Fig. 4, Fig. 10 and Fig. 5, this variant exhibits increased near-field specular leakage, degraded geometry reconstruction, and reduced fidelity in modeling near-field reflections compared to the variant with two separate sets of Gaussians, which we attribute to

optimization conflicts between geometric representation and local specular reflection when modeled within a single set.

Adaptive Mixing. We ablate the adaptive mixing mechanism in the specular shader by removing the learned global-local balancing and instead combining the global and local specular features by direct summation: $F_{\text{sum}}(\mathbf{p}) = F_{\text{global}}(\mathbf{p}) + F_{\text{local}}(\mathbf{p})$. Specular radiance is then predicted from $F_{\text{sum}}(\mathbf{p})$ together with the physical conditioning terms, $C_{\text{spec}}(\mathbf{p}) = f_{\Theta}(F_{\text{sum}}(\mathbf{p}), \rho(\mathbf{p}), \cos_{NV})$. As shown in Fig. 10, direct feature summation yields unstable view-dependent specular responses. This is because, for a given view, specular appearance is typically dominated by either far-field or near-field reflections, depending on visibility, rather than an equal contribution of both. Moreover, the relative importance of these components varies across viewpoints. Without adaptive mixing, direct summation fails to model this view-dependent effect, leading to reduced generalization to novel views.

Physically-Aware Conditioning. We ablate the physically-aware conditioning of the specular shader by removing all explicit physical terms from its inputs. Specifically, the roughness $\rho(\mathbf{p})$ and angular cosine term \cos_{NV} are discarded, and specular radiance is predicted solely from the global and local specular features: $C_{\text{spec}}(\mathbf{p}) = f_{\Theta}(F_{\text{global}}(\mathbf{p}), F_{\text{local}}(\mathbf{p}))$. As shown in Tab. 4 and Fig. 10, removing physical conditioning results in unstable and less plausible view-dependent specular behavior, indicating that explicit physical terms help regularize optimization and improve generalization to novel views. The improvement is relatively modest, likely because the expressive shader MLP and high-dimensional specular features can implicitly encode some view-dependent and roughness-related information through multi-view Gaussian splatting.

5 Conclusion

We have presented **Ref-DGS**, a reflective dual Gaussian splatting framework that enables efficient and high-quality modeling of reflective appearance without explicit ray tracing. The key insight of Ref-DGS is to decouple near-field specular reflection from surface geometry via a dual Gaussian scene representation, assigning local reflective interactions to a dedicated set of local reflection Gaussians while preserving stable and accurate surface reconstruction. By representing specular appearance using complementary global and local reflection features and predicting specular radiance with a lightweight, physically-aware adaptive mixing shader, Ref-DGS captures both far-field and near-field reflective effects within a rasterization-based pipeline.

Ref-DGS achieves state-of-the-art performance on reflective scenes in both surface reconstruction and novel view synthesis, while training substantially faster than ray-based Gaussian methods. Beyond improved visual/geometric quality and efficiency, our model demonstrates that explicitly separating near-field specular reflection from surface geometry is critical for stable and accurate modeling of complex view-dependent appearance. We believe this dual-representation perspective provides a useful insight for future extensions of Gaussian splatting toward more expressive modeling of view-dependent appearance.

References

- Jonathan T. Barron, Ben Mildenhall, Matthew Tancik, Peter Hedman, Ricardo Martin-Brualla, and Pratul P. Srinivasan. 2021. Mip-NeRF: A Multiscale Representation for Anti-Aliasing Neural Radiance Fields. In *Proceedings of the IEEE/CVF International Conference on Computer Vision (ICCV)*. 5855–5864.
- Jonathan T. Barron, Ben Mildenhall, Dor Verbin, Pratul P. Srinivasan, and Peter Hedman. 2022. Mip-NeRF 360: Unbounded Anti-Aliased Neural Radiance Fields. In *Proceedings of the IEEE/CVF Conference on Computer Vision and Pattern Recognition (CVPR)*. 5470–5479.
- Anpei Chen, Zexiang Xu, Andreas Geiger, Jingyi Yu, and Hao Su. 2022. Tensor4: Tensorial radiance fields. In *European conference on computer vision*. Springer, 333–350.
- Danpeng Chen, Hai Li, Weicai Ye, Yifan Wang, Weijian Xie, Shangjin Zhai, Nan Wang, Haomin Liu, Hujun Bao, and Guofeng Zhang. 2024. Pgsr: Planar-based gaussian splatting for efficient and high-fidelity surface reconstruction. *IEEE Transactions on Visualization and Computer Graphics* (2024).
- Hanlin Chen, Chen Li, Yunsong Wang, and Gim Hee Lee. 2023. Neusg: Neural implicit surface reconstruction with 3d gaussian splatting guidance. *arXiv preprint arXiv:2312.00846* (2023).
- Yue Fan, Ningjing Fan, Ivan Skorokhodov, Oleg Voynov, Savva Ignatyev, Evgeny Burnaev, Peter Wonka, and Yiqun Wang. 2025. Factored-neus: Reconstructing surfaces, illumination, and materials of possibly glossy objects. In *Proceedings of the Computer Vision and Pattern Recognition Conference*. 21317–21327.
- Sara Fridovich-Keil, Alex Yu, Matthew Tancik, Qinhong Chen, Benjamin Recht, and Angjoo Kanazawa. 2022. Plenoxels: Radiance Fields Without Neural Networks. In *Proceedings of the IEEE/CVF Conference on Computer Vision and Pattern Recognition (CVPR)*. 5501–5510.
- Jian Gao, Chun Gu, Youtian Lin, Zhihao Li, Hao Zhu, Xun Cao, Li Zhang, and Yao Yao. 2024. Relightable 3d gaussians: Realistic point cloud relighting with brdf decomposition and ray tracing. In *European Conference on Computer Vision*. Springer, 73–89.
- Wenhang Ge, Tao Hu, Haoyu Zhao, Shu Liu, and Ying-Cong Chen. 2023. Ref-neus: Ambiguity-reduced neural implicit surface learning for multi-view reconstruction with reflection. In *Proceedings of the IEEE/CVF International Conference on Computer Vision*. 4251–4260.
- Antoine Guédon, Diego Gomez, Nissim Maruani, Bingchen Gong, George Drettakis, and Maks Ovsjanikov. 2025. Milo: Mesh-in-the-loop gaussian splatting for detailed and efficient surface reconstruction. *ACM Transactions on Graphics (TOG)* 44, 6 (2025), 1–15.
- Antoine Guédon and Vincent Lepetit. 2024. SuGaR: Surface-Aligned Gaussian Splatting for Efficient 3D Mesh Reconstruction and High-Quality Mesh Rendering. In *Proceedings of the IEEE/CVF Conference on Computer Vision and Pattern Recognition (CVPR)*. 5354–5363.
- Binbin Huang, Zehao Yu, Anpei Chen, Andreas Geiger, and Shenghua Gao. 2024a. 2D Gaussian Splatting for Geometrically Accurate Radiance Fields. In *SIGGRAPH 2024 Conference Papers*. Association for Computing Machinery. doi:10.1145/3641519.3657428
- Binbin Huang, Zehao Yu, Anpei Chen, Andreas Geiger, and Shenghua Gao. 2024b. 2d gaussian splatting for geometrically accurate radiance fields. In *ACM SIGGRAPH 2024 conference papers*. 1–11.
- Yingwenqi Jiang, Jiadong Tu, Yuan Liu, Xifeng Gao, Xiaoxiao Long, Wenping Wang, and Yuexin Ma. 2024. GaussianShader: 3D Gaussian Splatting with Shading Functions for Reflective Surfaces. In *Proceedings of the IEEE/CVF Conference on Computer Vision and Pattern Recognition (CVPR)*. 5322–5332.
- Bernhard Kerbl, Georgios Kopanas, Thomas Leimkühler, and George Drettakis. 2023. 3D Gaussian splatting for real-time radiance field rendering. *ACM Trans. Graph.* 42, 4 (2023), 139–1.
- Jia Li, Lu Wang, Lei Zhang, and Beibei Wang. 2024. Tensordf: Roughness-aware tensorial representation for robust geometry and material reconstruction. *ACM Transactions on Graphics (TOG)* 43, 4 (2024), 1–13.
- Ruofan Liang, Huiting Chen, Chunlin Li, Fan Chen, Selvakumar Panneer, and Nandita Vijaykumar. 2023. Envird: Implicit differentiable renderer with neural environment lighting. In *Proceedings of the IEEE/CVF International Conference on Computer Vision*. 79–89.
- Zhihao Liang, Qi Zhang, Ying Feng, Ying Shan, and Kui Jia. 2024. GS-IR: 3D Gaussian Splatting for Inverse Rendering. In *Proceedings of the IEEE/CVF Conference on Computer Vision and Pattern Recognition (CVPR)*. 21644–21653.
- Yuan Liu, Peng Wang, Cheng Lin, Xiaoxiao Long, Jiepeng Wang, Lingjie Liu, Taku Komura, and Wenping Wang. 2023. Nero: Neural geometry and brdf reconstruction of reflective objects from multiview images. *ACM Transactions on Graphics (TOG)* 42, 4 (2023), 1–22.
- Xiaoyang Lyu, Yang-Tian Sun, Yi-Hua Huang, Xiuzhe Wu, Ziyi Yang, Yilun Chen, Jiangmiao Pang, and Xiaojuan Qi. 2024. 3dgsr: Implicit surface reconstruction with 3d gaussian splatting. *ACM Transactions on Graphics (TOG)* 43, 6 (2024), 1–12.
- Ben Mildenhall, Pratul P. Srinivasan, Matthew Tancik, Jonathan T. Barron, Ravi Ramamoorthi, and Ren Ng. 2020. NeRF: Representing Scenes as Neural Radiance Fields for View Synthesis. In *ECCV*.
- Thomas Müller, Alex Evans, Christoph Schied, and Alexander Keller. 2022. Instant Neural Graphics Primitives with a Multiresolution Hash Encoding. *ACM Trans. Graph.* 41, 4, Article 102 (July 2022), 15 pages. doi:10.1145/3528223.3530127
- Dor Verbin, Peter Hedman, Ben Mildenhall, Todd Zickler, Jonathan T. Barron, and Pratul P. Srinivasan. 2022. Ref-NeRF: Structured View-Dependent Appearance for Neural Radiance Fields. *CVPR* (2022).
- Fangjinhua Wang, Marie-Julie Rakotosaona, Michael Niemeyer, Richard Szeliski, Marc Pollefeys, and Federico Tombari. 2024. Unisdf: Unifying neural representations for high-fidelity 3d reconstruction of complex scenes with reflections. *Advances in Neural Information Processing Systems* 37 (2024), 3157–3184.
- Peng Wang, Lingjie Liu, Yuan Liu, Christian Theobalt, Taku Komura, and Wenping Wang. 2021. NeuS: Learning Neural Implicit Surfaces by Volume Rendering for Multi-view Reconstruction. *NeurIPS* (2021).
- Tao Xie, Xi Chen, Zhen Xu, Yiman Xie, Yudong Jin, Yujun Shen, Sida Peng, Hujun Bao, and Xiaowei Zhou. 2025. EnvGS: Modeling View-Dependent Appearance with Environment Gaussian. In *Proceedings of the IEEE/CVF Conference on Computer Vision and Pattern Recognition (CVPR)*. 5742–5751.
- Ziyi Yang, Xinyu Gao, Yang-Tian Sun, Yihua Huang, Xiaoyang Lyu, Wen Zhou, Shaohui Jiao, Xiaojuan Qi, and Xiaogang Jin. 2024. Spec-gaussian: Anisotropic view-dependent appearance for 3d gaussian splatting. *Advances in Neural Information Processing Systems* 37 (2024), 61192–61216.
- Yuxuan Yao, Zixuan Zeng, Chun Gu, Xiattian Zhu, and Li Zhang. 2025. Reflective Gaussian Splatting. In *International Conference on Representation Learning*, Y. Yue, A. Garg, N. Peng, F. Sha, and R. Yu (Eds.), Vol. 2025. 68695–68711. https://proceedings.iclr.cc/paper_files/paper/2025/file/abf3682c9cf9245a0294a4bebe4544ff-Paper-Conference.pdf
- Keyang Ye, Qiming Hou, and Kun Zhou. 2024. 3d gaussian splatting with deferred reflection. In *ACM SIGGRAPH 2024 Conference Papers*. 1–10.
- Mulin Yu, Tao Lu, Linning Xu, Lihan Jiang, Yuanbo Xiangli, and Bo Dai. 2024a. GSDf: 3DGS Meets SDF for Improved Neural Rendering and Reconstruction. In *Advances in Neural Information Processing Systems*, A. Globerson, L. Mackey, D. Belgrave, A. Fan, U. Paquet, J. Tomczak, and C. Zhang (Eds.), Vol. 37. Curran Associates, Inc., 129507–129530. doi:10.52202/079017-4115
- Zehao Yu, Torsten Sattler, and Andreas Geiger. 2024b. Gaussian Opacity Fields: Efficient Adaptive Surface Reconstruction in Unbounded Scenes. *ACM Transactions on Graphics* (2024).
- Wenyuan Zhang, Jimin Tang, Weiqi Zhang, Yi Fang, Yu-Shen Liu, and Zhizhong Han. 2025c. MaterialRefGS: Reflective Gaussian Splatting with Multi-view Consistent Material Inference. In *The Thirty-ninth Annual Conference on Neural Information Processing Systems*.
- Youjia Zhang, Anpei Chen, Yumin Wan, Zikai Song, Junqing Yu, Yawei Luo, and Wei Yang. 2025a. Ref-gs: Directional factorization for 2d gaussian splatting. In *Proceedings of the Computer Vision and Pattern Recognition Conference*. 26483–26492.
- Ziyu Zhang, Binbin Huang, Hanqing Jiang, Liyang Zhou, Xiaojuan Xiang, and Shuhan Shen. 2025b. Quadratic Gaussian Splatting: High Quality Surface Reconstruction with Second-order Geometric Primitives. In *Proceedings of the IEEE/CVF International Conference on Computer Vision (ICCV)*. 28260–28270.
- Zuo-Liang Zhu, Jian Yang, and Beibei Wang. 2025. GS-ROR²: Bidirectional-guided 3DGS and SDF for Reflective Object Relighting and Reconstruction. *ACM Transactions on Graphics (TOG)*. doi:10.1145/3759248

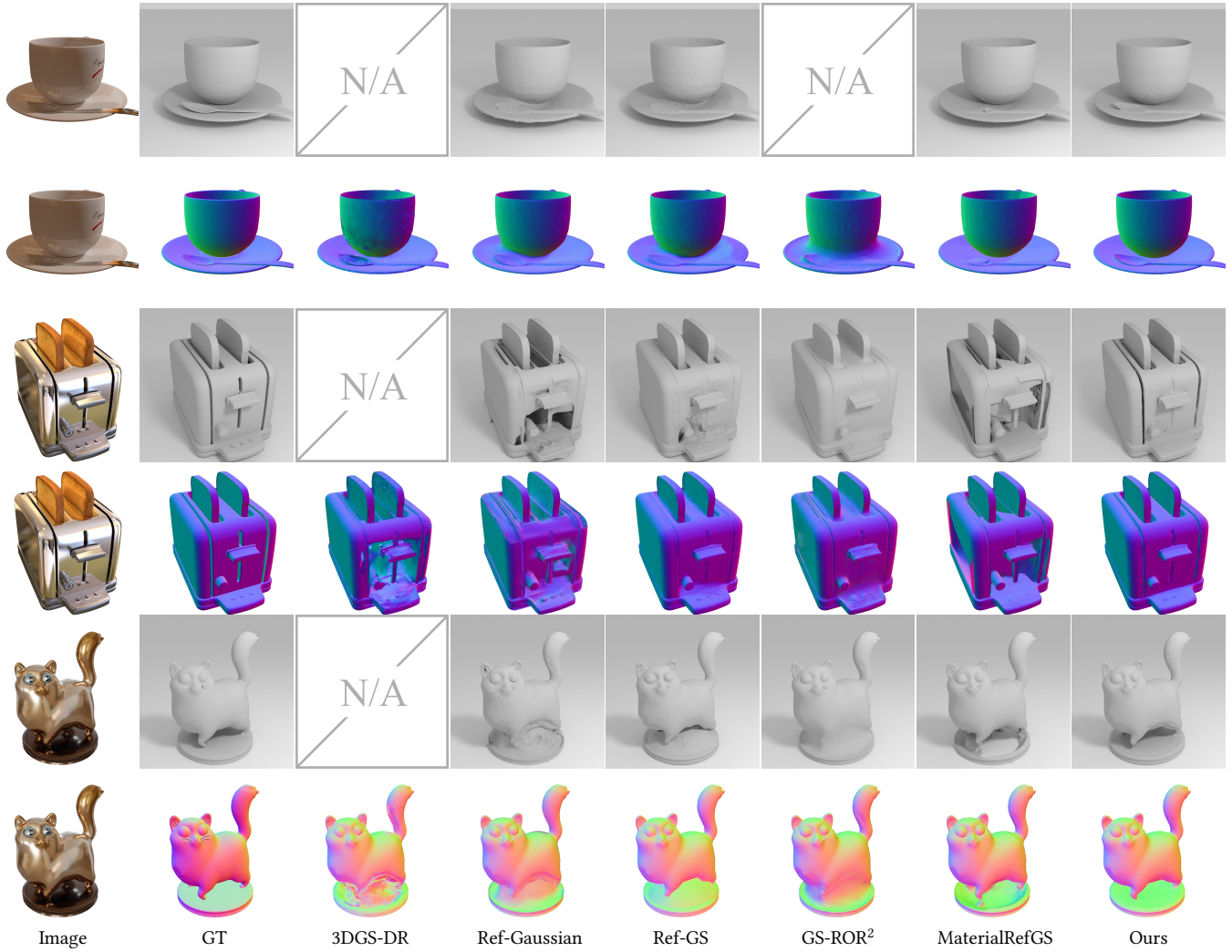


Fig. 6. Qualitative surface reconstruction results (meshes and normals) on the ShinySynthetic (coffee, toaster) and GlossySynthetic (cat) datasets.

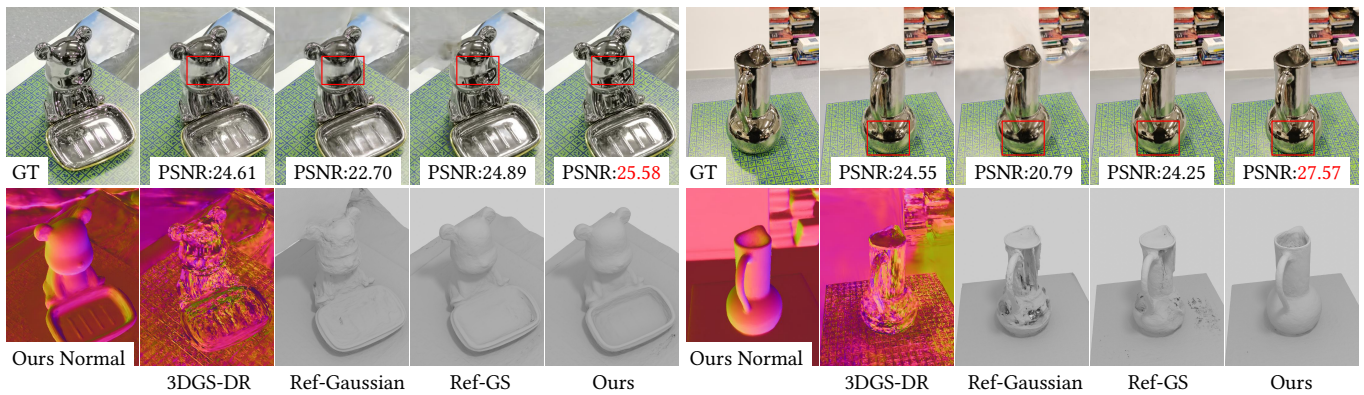


Fig. 7. Qualitative rendering quality and surface reconstruction on the GlossyReal (bear, vase) dataset.

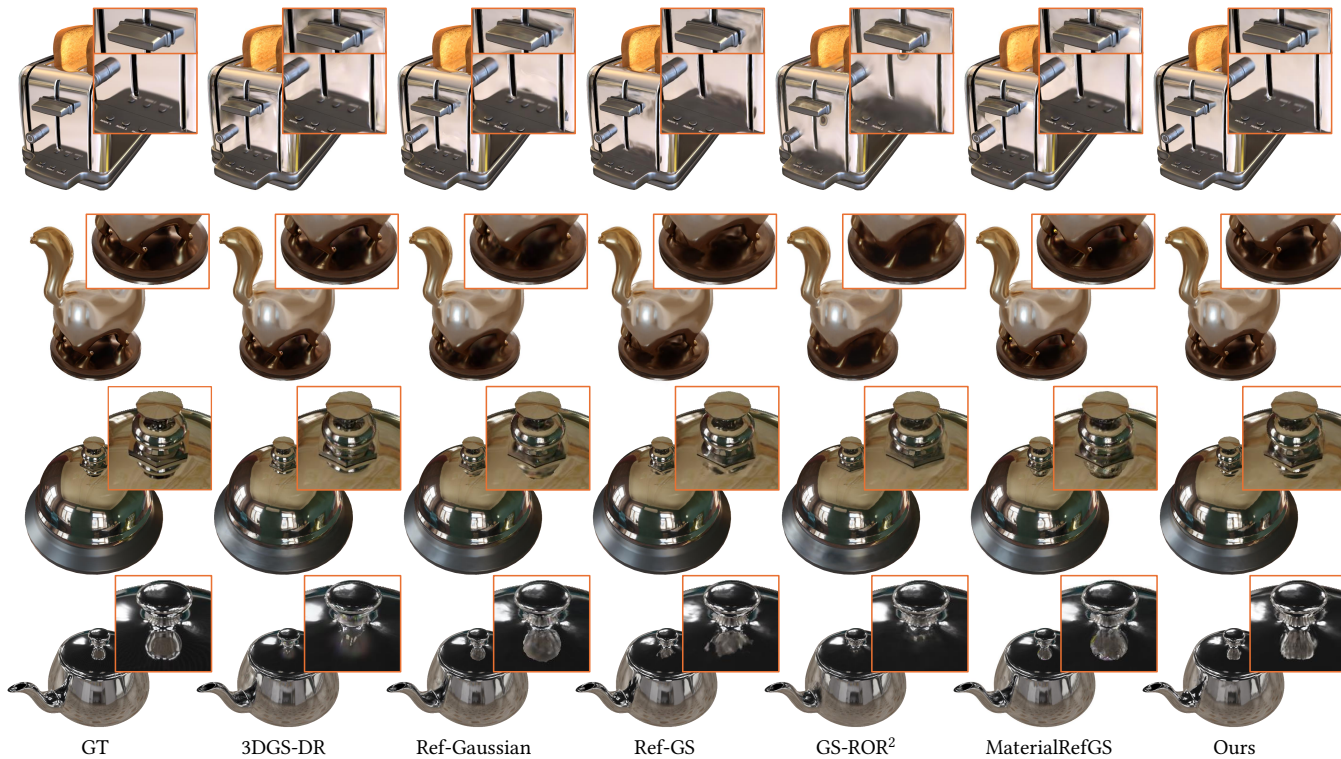


Fig. 8. Qualitative NVS results on the ShinySynthetic (toaster) and GlossySynthetic (cat, tbell, teapot) datasets.

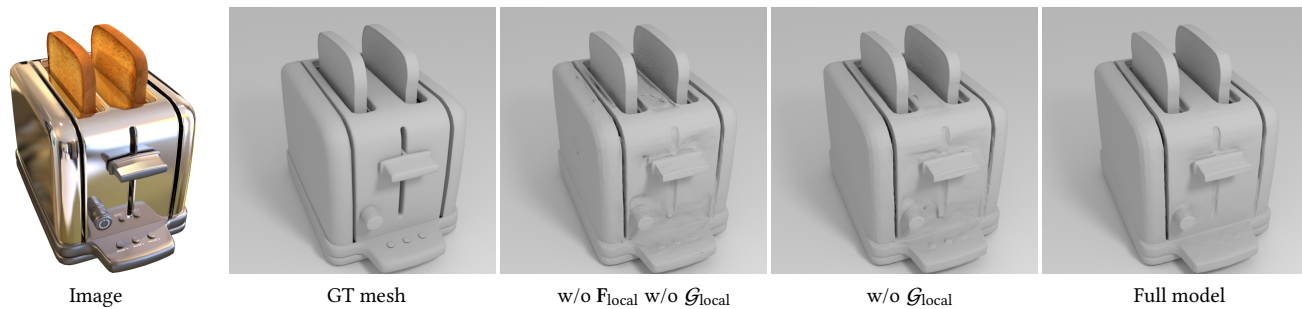


Fig. 9. Ablation study on surface reconstruction.

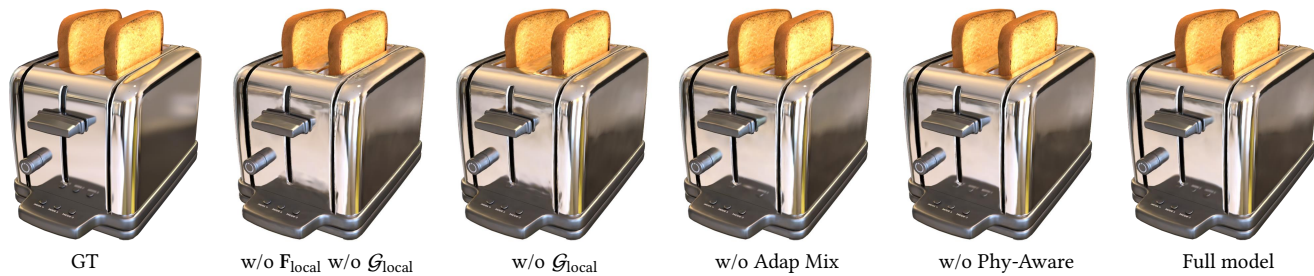


Fig. 10. Ablation study on novel view synthesis.

A Additional Results

In this section, we present additional results on a real-world dataset and scene decomposition. Specifically, we show qualitative results on the Mip-NeRF 360 dataset and additional scene decomposition examples to illustrate how our method handles near-field reflections. These results provide further insight into the behavior of our approach in surface reconstruction, rendering, and material decomposition under challenging reflective conditions.

A.1 Mip-NeRF 360 Dataset

Fig. 11 shows qualitative results and normal map visualizations on the Mip-NeRF 360 dataset for the garden and counter scenes. We compare our method with Ref-Gaussian and Ref-GS. In the garden scene, the vase placed on the table produces clear near-field reflections on the tabletop. Existing methods tend to introduce concave artifacts in this region to fit the reflected appearance, whereas our method reconstructs a flatter and more geometrically consistent surface. Consequently, the recovered surface normals are more coherent, with fewer distortions in the reflection region. In the counter scene, the stainless steel bowl exhibits strong specular reflections, and the presence of many surrounding objects leads to complex illumination effects. Under these conditions, our model yields a cleaner surface and more stable surface normals for the stainless steel bowl than the baseline methods.

A.2 Scene Decomposition

Fig. 12 shows additional qualitative results of scene decomposition in the presence of strong near-field reflections. Our method achieves a cleaner separation of the diffuse component, specular reflection component, and surface roughness compared to prior approaches. In regions affected by strong near-field reflections, existing methods tend to misattribute reflection signals to the diffuse component. Since surface reconstruction primarily relies on the diffuse signal, this leakage directly degrades geometry quality, leading to incorrect surface shape and unstable surface normals. In contrast, our method suppresses such leakage, preserving a more consistent diffuse estimate that better supports geometry reconstruction. Moreover, near-field reflections also interfere with roughness estimation in prior methods. When the specular appearance cannot be explained by the environment map, these methods tend to increase surface roughness, causing the reflection to be matched through higher-level mipmap sampling of the environment map. This leads to inflated roughness values and blurred reflection appearance. Our approach produces more stable and physically plausible roughness estimates, reducing the influence of reflection artifacts on the material decomposition.

B Optimization

We optimize the parameters of the geometry Gaussians \mathcal{G}_{geo} , the local reflection Gaussians $\mathcal{G}_{\text{local}}$, the spherical mipmap \mathbf{M} , and the neural shader f_{θ} . The loss function is

$$\mathcal{L} = \mathcal{L}_c + \lambda_n \mathcal{L}_n + \mathcal{L}_\alpha + \lambda_{\text{prior}} \mathcal{L}_{\text{prior}}. \quad (10)$$

The photometric and normal consistency losses follow 2DGS [Huang et al. 2024a]:

$$\mathcal{L}_c = (1 - \lambda) \mathcal{L}_1 + \lambda \mathcal{L}_{\text{SSIM}}, \quad \mathcal{L}_n = \sum_i \omega_i (1 - \mathbf{n}_i^\top \mathbf{N}). \quad (11)$$

The opacity regularization is defined using binary cross entropy,

$$\mathcal{L}_\alpha = - \sum_i [\alpha_i \log \hat{\alpha}_i + (1 - \alpha_i) \log(1 - \hat{\alpha}_i)], \quad (12)$$

where $\hat{\alpha}_i$ denotes the predicted opacity and α_i denotes the ground-truth opacity, and this term is applied only to synthetic datasets.

The prior term consists of a depth prior

$$\mathcal{L}_{\text{depth}} = \min_{s,t} \|sD + t - D_{\text{ref}}\|_2^2, \quad (13)$$

where s and t denote a scale and a translation factor used to align the predicted depth with the reference depth, and a normal prior

$$\mathcal{L}_{\text{normal}} = \|\mathbf{N} - \mathbf{N}_{\text{ref}}\|_1 + \lambda \left(1 - \frac{\mathbf{N} \cdot \mathbf{N}_{\text{ref}}}{\|\mathbf{N}\| \|\mathbf{N}_{\text{ref}}\|} \right), \quad (14)$$

with $\mathcal{L}_{\text{prior}} = \mathcal{L}_{\text{depth}} + \mathcal{L}_{\text{normal}}$. Here D and \mathbf{N} denote the predicted depth and normal, respectively, while D_{ref} and \mathbf{N}_{ref} are obtained from VGGT for synthetic datasets and from Metric3d v2 for real-world datasets.

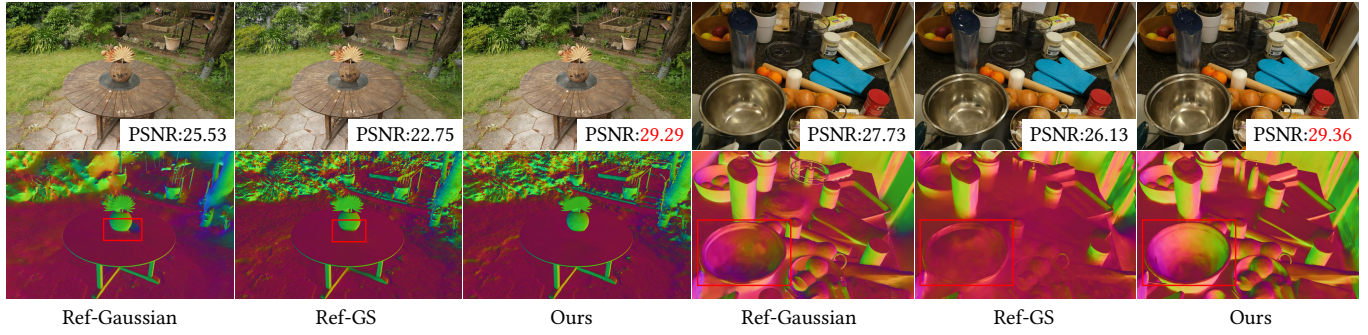


Fig. 11. Qualitative rendering quality and normal map results on the Mip-NeRF 360 dataset for the garden (left) and counter (right) scenes. Best viewed with zoom in.



Fig. 12. Scene decomposition under strong near-field reflections. Our method separates the diffuse component, specular reflection component, and surface roughness in regions dominated by near-field reflections. Best viewed with zoom in.